Thermo-electro-mechanical aging and degradation of conductive PLA/CB composite

J. Crespo-Miguel[a], D. Garcia-Gonzalez[a,*], G. Robles[b], M. Hossain[c], J.M. Martinez-Tarifa[b], A. Arias [a,*]

[a] Department of Continuum and Structural Analysis, University Carlos III of Madrid, Avda. Universidad 30, Leganés 28911, Madrid, Spain

[b] Department of Electrical Engineering, University Carlos III of Madrid, Avda de la Universidad 30, Leganés 28911, Madrid, Spain

[c] Zienkiewicz Centre for Computational Engineering, College of Engineering, Swansea University, SA1 8EN, United Kingdom

* Corresponding authors

E-mail addresses: danigarc@ing.uc3m.es (D. Garcia-Gonzalez), aariash@ing.uc3m.es (A.Arias)

Abstract: Conductive polymeric composites consist of a polymeric matrix filled with conductive particles, providing electrical properties to a naturally insulating material. Their use in material extrusion printers provides great flexibility to geometrical design functional components. However, the degradation of their mechanical behavior during and after the application of electric currents is still absent in the literature. The flow of electric currents induces material heating affecting the strength, and mechanical deformation alters the electric properties leading to bilateral dependences. These processes evolve during the application of electric fields and may degrade the material behavior permanently. In this work, we address these questions taking as baseline material a 3D printed conductive Polylactic Acid (PLA)/ Carbon Black (CB) composite. We performed multi-physical characterizations on samples with different printing orientation and length evaluating: i) electric behavior under direct current (DC) regime and a wideband analysis by a Frequency Response Analysis; ii) thermo-electrical behavior studying the temperature field evolution under applied electric fields; iii) thermo-mechanical behavior under uniaxial tension for different testing temperatures; iv) thermo-electrical aging/degradation effects on the mechanical behavior. The study considers a wide range of electric fields (from 180 V/m to 600 V/m) and temperatures (from 25° to 130 °C). The results show enhanced electrical conductivity and mechanical stiffness when using a printing orientation parallel to the electro-mechanical loading. This coupled response is highly influenced by thermal effects due to Joule heating, especially when surpassing the glass transition and cold crystallization temperatures of the composite. The occurrence of such phase transitions governs the material degradation by promoting the growth of mesostructural pores during heating cycles arising from the application of electric fields. The obtained results are essential to unravel changes in mechanical properties when standing for continuous electric conduction and provide an experimental background for the lifetime expectance for the devices and possible thermo-electro-mechanical failure.

Keywords: Smart material, 3D printing, Conductive composites, Multifunctional characterization

1. Introduction

The conceptualization of structural components in the current industry is experiencing an unprecedented change of paradigm. In this regard, new materials are emerging to provide other functionalities while preserving certain structural functions. An exciting example is due to conductive polymeric composites, that allow for applications where electrical current flow is needed through mechanical components. These multifunctional materials stand out as great candidates to substitute conventional conductive materials for applications such as sensors [1-8], biomedical devices [8-12], flexible electronics [13-14], electrodes in electroactive devices [15] and electromagnetic shielding [16-17], among others. Except for a specific type of synthetic polymers called Intrinsically Conductive Polymers (ICPs) [18], good conductive properties require the addition of conductive particles to a polymeric matrix [19-23].

The wide range of possibilities for the polymeric matrices, along with their diverse mechanical behaviors, open an enormous field for design purposes. A major feature limiting the conceptualization of new smart components is related to the manufacturing process. Processes such as traditional casting [24] or extruding techniques [25] present several limitations. For instance, the need of a mold for casting, or the limitation to a constant cross section for extruding, hinder the manufacturing of complex geometries. In addition, achieving a selective heterogeneous electrical response is complicated due to the constant feedstock flow in these processes. Such limitations can be overcome using advanced additive manufacturing (AM) or 3D printing techniques. Within AM materials, conductive thermoplastics are one of the best solutions for manufacturing conductive-structural components. They can be printed with FFF machines [26-27], allowing the manufacturing of complex geometries, while exhibiting a good strength-cost ratio [28-29]. In addition, FFF technique is one of the most mature technologies regarding Multi Material Additive Manufacturing, allowing the manufacturing of conductive structures embedded in an insulator [6,30]. Thus, a selective heterogeneous electrical response can be achieved, contrary to casting or extruding processes.

Conductive thermoplastic composites consist of a thermoplastic matrix reinforced with conductive particles, e.g., carbon blacks or carbon nanotubes, that create conductive pathways within them. Despite the mentioned advantages of these printed composites, they present several complexities associated to their microstructural compositions and manufacturing processes. From an electrical point of view, the conductivity of these materials can be described using the percolation theory [17,31,32] that defines, in a stochastic manner, the electric behavior accounting for the creation and destruction of conductive paths. Following this theory, there are several factors that can change drastically the conductivity, such as the size and shape of the conductive particles [33], the aspect ratio of the fillers [20,33,34], the volume fraction of the filler [32-33] or its proper dispersion within the matrix [32,35]. From a mechanical perspective, the thermoplastic nature of the matrix leads to nonlinear mechanical behavior, viscoelastic and viscoplastic responses [36], among others [37]. In addition, porosity and microstructural anisotropy are present while using FFF techniques. The latter is extremely relevant, as it does not only determine the mechanical behavior [38] but also influences both electrical and thermal ones. Finally, as an extra source of complexity, once an electrical current flows through a material, it gets heated due to Joule effect. This thermal response is, in turn, coupled to the mechanical response via stiffness modulation, and to the electrical behavior via resistivity temperature dependence and thermal expansion [39].

Recent works have studied multifunctional responses of 3D printed conductive thermoplastics, mainly focusing on the electro-mechanical behavior of these materials when used as strain [4], force [1] or flex sensors [3], obtaining the variation of resistivity when they deform. Most of these studies focused on Polylactic Acid (PLA) matrices reinforced with different fillers, thanks to the easy manufacturing, upstanding printing behavior and good ratio between mechanical properties and cost of PLA feedstocks [28,40,41]. The principal conductive fillers employed for these filaments are carbon-based particles, such as Carbon Black (CB) nano-powder or Carbon Nanotubes (CNTs). Previous studies focused on the manufacturing of customized conductive

PLA composites and provided a general electro-mechanical characterization of each blend, such as PLA-PMMA-PFG [42], PLA/TPU-GnP [43] or PLA/MWCNT's [44]. A relevant work is due to Ke Dong et al [26], that manufactured electrical responsive auxetic structures. Regarding the thermo-electrical behavior, some previous works have addressed the study of different materials such as carbon fiber-epoxy composites [45], Graphene/PLA composites [46] or polyvinyl acetate/graphite adhesive [47]. Most of these works neither present any specific analysis of the resistance dependence on temperature [45], nor thermal stabilization between voltage/power steps [46-47].

In the present study we take CB-PLA conductive composite from Proto-Pasta® as the baseline material. This material has been studied from different perspectives. The mechanical response under uniaxial loading at room temperature was studied by J. Beniak et al [48]. From an electro-chemical point of view, the use of this material as electrode was studied [27,49,50]. In addition, from a purely electric perspective, resistivity and impedance were studied by different authors, without considering the influence of printing orientation [49-51]. In addition, a previous work by the authors analyzed its response under low applied electric fields (maximum of 180 V/m) with a fixed sample length (165mm), providing a first approach to understand its multifunctional couplings [39]. A proper understanding of electro-thermo-mechanical coupled behavior of conductive PLA composites at higher fields is essential to open the current sensor approach to more potential uses for the 3D printed thermoplastic polymers.

In this work, we aim to study the thermo-electrical behavior of 3D printed conductive PLA composites and how this response affects its mechanical counterpart when varying the printing orientation and length of the samples. These geometrical features are especially relevant as the location of voids changes drastically the inherent conductive paths of the composite. With the aim of studying how this material will behave in a real working scenario, we have first evaluated the influence of thermo-electric loading on its mechanical response and the different bilateral couplings. After a comprehensive characterization of these responses, we have evaluated the material degradation after thermo-electrical loading. In this regard, we have demonstrated that the application of electric fields generates heating leading to phase transitions within the polymeric matrix, which significantly impacts (degrades) its mechanical performance. A major gap in the current literature that prevents a further use of these materials is the understanding of their electro-thermal response over time for a wide range of temperatures (previous and after glass transition and cold crystallization). This knowledge is essential to unravel the electro-mechanical aging when standing for a continuous electric conduction. We provide a series of multi-physical experimental procedures for characterizing the material behaviors that significantly affect its use in conductive structural components. To this end: i) an electrical analysis under direct current (DC) was performed (i.e., room temperature), as well as an analysis under variable frequency signals; ii) an analysis of temperature evolution over time for samples heated by Joule effect was carried out; iii) uniaxial tensile tests were performed for different testing temperatures, to simulate the mechanical response on the material when heated by Joule effect; iv) uniaxial tensile tests were conducted on samples previously heated, to analyze the thermo-mechanical aging of the material. Overall, the results presented in this study will facilitate at opening new applications for these materials, from a sensor perspective to a wider range of devices that require domestic power ranges to operate. In this regard, the present work provides an experimental background for the degradation mechanisms of this material and possible thermo-electro-mechanical failure, trying to characterize their limits.

2. Materials and methods

2.1 Baseline material

Conductive PLA composite was purchased to ProtoPasta, WA, USA. A differential scanning calorimetry (DSC) test was performed (TA Instruments DSC-Q200, DE, USA) to obtain the main transition temperatures of the polymer, Fig.1. The glass transition temperature (T_g) was found at 62ºC, following norm ISO 11357-2. A two-step crystallization can be found after this glass transition. This effect has been studied in the literature [52-53], and it is caused by the formation of two different crystallized phases. Firstly, α'[52] phase is formed, appearing at temperatures below 120ºC for conventional PLA. Secondly, α phase is formed in parallel to the before mentioned α' phase, appearing at temperatures higher than 120ºC for conventional PLA. In the case of the PLA/CB used in this work, these crystallizations present their peaks at lower temperatures, 95ºC for $T_{\alpha'}$ and 110ºC for T_{α}. Finally, the melting temperature (T_m) was found at 151ºC.
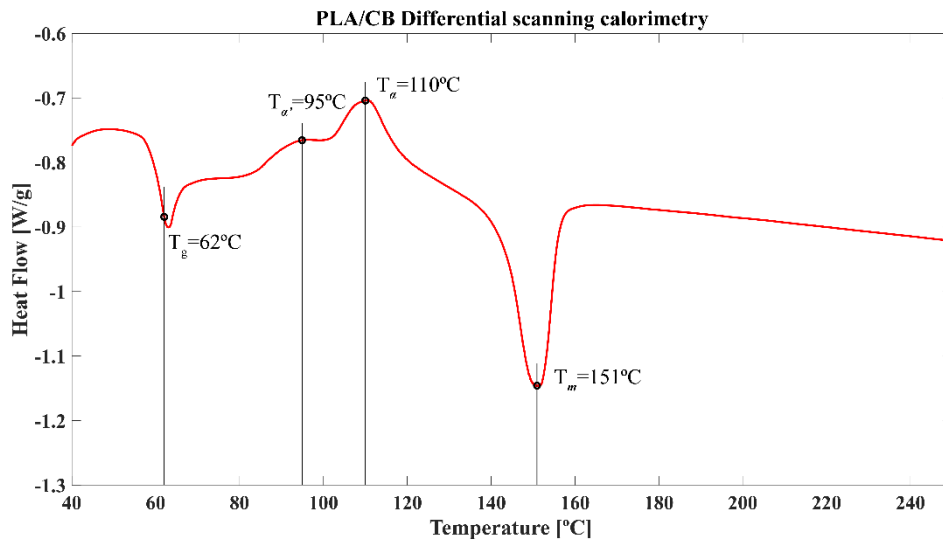

Figure 1: Differential scanning calorimetry of PLA/CB composite from 40ºC to 250ºC. The transition temperatures are highlighted. From left to right: i) glass transition temperature (T_g); ii) crystallization temperature of α' form ($T_{\alpha'}$); iii) crystallization temperature of α form (T_{α}); iv) melting temperature (T_m).

A field emission scanning electron microscopy (FESEM) was used (FEI Teneo, OR, USA), obtaining both mesostructure and microstructure of the material. The different samples were submerged in liquid nitrogen to embrittle them. Then, they were cut by a high velocity impact. The mesostructure of a longitudinal sample is shown in Fig. 2b, along with a diagram of the voids shape depending on the printing orientation, in Fig. 2c. The microstructure of PLA/CB is shown in Fig. 2a. This material exhibits a CB mass ratio of 53% whereas it represents the 26.5% in volume [39]. The porosity average at the mesostructural level is 1.44%, whereas it is 27.5% at the microstructural level. The void and particle contents were estimated via image processing using the software ImageJ.
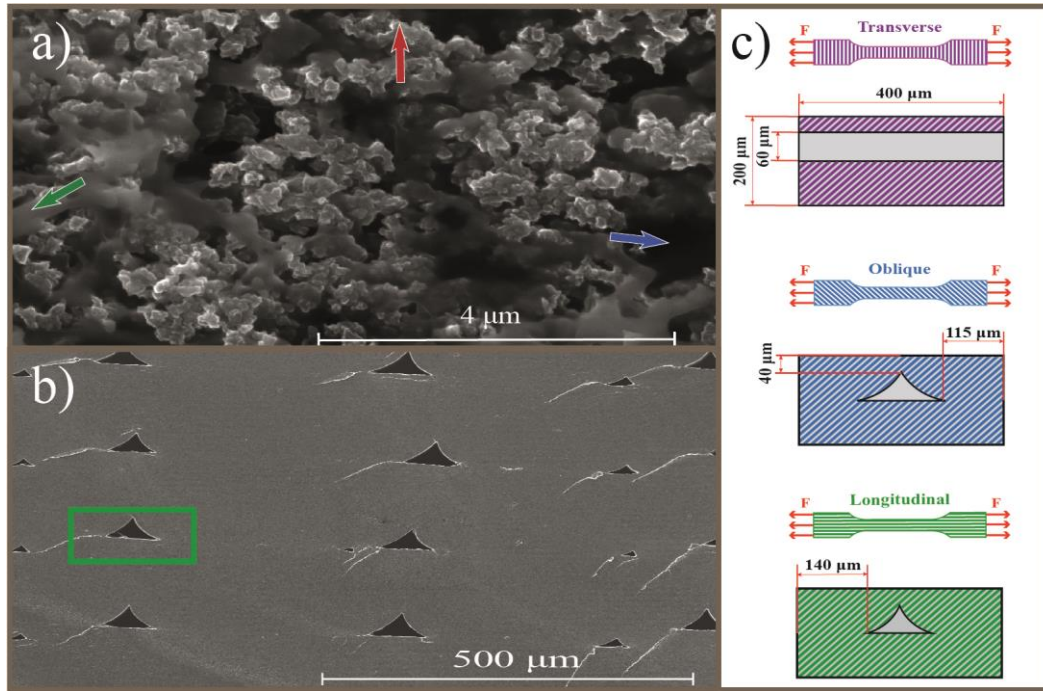
Figure 2: a) SEM of the microstructure of a printed PLA/CB sample. The image represents a region within the filament (not at the interphase of the filaments). Green arrow points the polymeric phase; red arrow points CB particles; and blue arrow points the voids. b) SEM image of the mesostructure of a longitudinal sample, highlighting a representative rectangle of the void size and location. c) Schematic representation of the void sizes in the cross section for every printing orientation type. Transverse in purple, oblique in blue and longitudinal in green.

One of the main aims of this contribution is to study how the voids' distribution impacts the electro-thermo-mechanical performance of 3D printed conductive composites. We consider two crucial parameters that play a relevant role in both voids' distribution and quantity: the printing orientation and the length of the samples. To conduct such a study, we manufactured different rectangular samples accounting for three lengths and three printing directions. The sample dimensions considered were: 82.5x13x3mm for the shortest samples (1L); 165x13x3mm for the medium ones (2L); and 227x13x3mm for the longest ones (2.75L). For each sample length, the printing directions considered were: longitudinal (0º), transverse (90º) and oblique (±45º). Every sample was manufactured using a Prusa i3mk3s printer. The main printing parameters considered were: line width of 0.4 mm, layer height of 0.2 mm, printing temperature of 230ºC, build plate temperature of 60ºC, infill density of 100% and a printing speed of 30 mm/s.

2.2 Methods

In the present work a multi-physical experimental campaign is performed to 3D printed PLA/CB samples, to characterize the thermo-electro-mechanical behaviors of this composite. To this end: i) an electrical analysis is carried out measuring the direct current (DC) resistance and conducting a Frequency Response Analysis (FRA). Thus, the influence of the printing orientation, samples length and applied frequency on their equivalent circuits is evaluated; ii) the analysis of the temperature field over time for samples heated by Joule effect was performed. The electric signal was applied by means of a DC power source, while the temperature profile was measured using an infrared (IR) camera; iii) uniaxial tensile tests were carried out for different testing temperature conditions, to simulate the mechanical response on the material when heated by Joule effect; iv) uniaxial tensile tests were conducted on samples

previously subjected to DC voltages along time, to analyze the thermo-mechanical aging of the material.

2.2.1 Electric behavior

The purely electrical response of the material at room temperature was measured: i) at DC regime; ii) and varying frequency current regime. Firstly, the pure resistance of the samples was measured by means of a commercial ohmmeter, testing five samples for each printing orientation and length. Secondly, a Frequency Response Analysis was performed using a Solartron 1260 spectrum analyzer. This system provides the impedance in a broadband of frequencies. Samples were excited with a 30mV peak sinusoidal voltage for a variable frequency range between 0.2 Hz and 0.1 MHz with 20 points per decade. Once the impedances are obtained, the impedance (Z) versus frequency (f) curves can be fitted to that from one electric equivalent circuit using "Zview" commercial software. To quantify the electrical characteristics from each sample type, a broadband adjustment of the FRA data to an equivalent network has been done between 40 Hz and 0.1 MHz. The different samples had a constant cross section of 13x3 mm. The samples were wired by gluing copper cables to the ends of the samples, using a conductive paint based on carbon black (Bare Conductive, UK).

2.2.2 Thermo-electric behavior

To study the thermal response of Proto-Pasta® conductive PLA when subjected to an electric current, a wide range of DC voltages was applied to the samples. We consider a total of nine conditions according to: the printing orientations (transverse, oblique and longitudinal) and geometrical lengths (1L, 2L and 2.75L). The samples' wiring process was the same as performed in the previous section.

For each test, the applied voltage was imposed until reaching temperature and current stabilization: changes below 0.5ºC and 0.5mA between consecutive measurements. Once stabilization was reached, the sample was cooled down to room temperature to repeat the same process with a higher voltage. The values of the DC voltages were the same for samples with equal length. To optimize the study, the same voltage was simultaneously applied to three samples (longitudinal, oblique and traverse) measuring their consumed current by means of three commercial ammeters. Initially, the consumed power is high, due to the simultaneous current from the three samples, so a high-power DC source was used, EA-PS 9500-90 3U.

The temperature field of the samples during the test was measured using a Fluke IR camera (Fluke Ti480 PRO), taking a picture every 5 minutes until stabilization, considering an emissivity of the material of 0.95. The DC applied voltages depend on the length of the sample. For 1L samples, we used voltages from 25 V to 45 V. For 2L samples, the voltages used ranged from 30 V to 90 V. Finally, for 2.75L samples the voltages ranged from 50 V to 110 V. These voltage ranges were chosen to reach equivalent heating in the samples independently of their length.

2.2.3 Thermo-electro-mechanical behavior

This section explores the impact of i) temperature and ii) thermo-electric aging on the mechanical behavior of 3D-printed conductive PLA. For this, quasi-static uniaxial tensile tests were performed on: i) virgin samples at different testing temperatures; and ii) samples previously heated by Joule effect.

To this end, in the first set of experiments, the conductive PLA samples are mechanically tested under uniaxial tension while imposing different testing temperatures. The temperatures chosen are those reached due to Joule heating when applying the voltages considered in 5.2 section. The first temperature selected was room temperature (25ºC), to represent the mechanical behavior of each component outside the electrical working regime. To represent the average of maximum temperatures reached when applying a 30V electric potential to each printing orientation type, we also considered a testing temperature of 50ºC. This value is below PLA

glass transition temperature. To represent the average of maximum temperatures reached when applying a 60V electric potential to each printing orientation type, we selected a temperature of 80ºC. This value corresponds to a temperature above the PLA glass transition. Finally, 130ºC was chosen for being the average of maximum temperatures reached when applying a 90V electric potential to each printing orientation type. This value has a special interest, as Joule heating at 90V shows a clear variation of material's electrical behavior.

To perform these thermo-mechanical tests, we used a universal testing machine (Instron 34TM-5®), with a load cell of 5kN and wedge action grips of 5 kN. This setup was equipped with an climatic chamber to impose testing temperatures during the experiment. To ensure a correct temperature stabilization in the whole sample, it was kept at the testing temperature ten minutes before the start of an experiment. These tests are performed on samples manufactured with different printing orientations, i.e., longitudinal, oblique and transverse. To ensure repeatability, we conducted three repetitions for each experimental condition. The tests were performed at a strain rate of 10^{-3} s^{-1} to impose quasi-static conditions avoiding adiabatic heating. Following the recommendations of ISO 527-1:2019.

Moreover, for the second set of experiments, we evaluated the thermo-electrical aging of the samples in terms of their mechanical properties, i.e., how electric load cycles can alter the mechanical properties of a 3D printed sample. To this end, samples manufactured with the three different printing orientations were electrically heated until stabilization with applied voltages of 30, 60, and 90V. After reaching temperature stabilization, the samples were cooled down at room temperature. These thermally degraded samples were then tested under quasi-static uniaxial tensile conditions using the same experimental setup that for the thermo-mechanical tests, but this time imposing room temperature conditions. For the thermo-mechanical testing, we conducted three repetitions for each experimental condition to ensure repeatability.

Every sample had the same shape as the ones used for electrical and thermo-electrical experiments, considering only 2L samples for this section.

3. Results and discussion

3.1 Electric behavior

This section presents an electrical analysis of the samples' resistance under variable frequency signals. To this end, we show a Frequency Response Analysis, FRA, at room temperature. This is achieved by applying variable frequency low-magnitude voltages (bellow 9V) to non-degraded samples for all lengths and printing directions. This allows predicting the electrical behavior of the samples when subjected to higher voltages in electro-thermal tests for some possible applications where DC signals are not used.

The FRA results for each printing direction are shown in Fig. 3. Firstly, in Fig. 3a, apparent impedivity modulus ($|z_a|$) are presented, in which the apparent impedivity is defined as the normalized value of the impedance modulus ($|Z|$) with respect to length and area ($|z_a|=|Z|·A/L$). The solid lines represent the average response of the different sample lengths, while the shaded area represents the maximum dispersion. In Fig. 3b the phase angle of the impedance is shown. This value represents the angle between capacitive/inductive and purely resistive responses.

The material presents a slight capacitive behavior for frequencies between 0.2 Hz and 40 Hz, where the phase angle, θ, reaches maximum values, near 4º, for 1Hz. Once this frequency range is left behind, the material behavior is mainly resistive, with a phase angle close to 0º, this fact matches with impedance analysis in the literature [51]. The impedance response of the material from 40Hz to 0,1 MHz, independently of the printing orientation, can be modeled as an equivalent resistance. The values for the mentioned equivalent resistance, normalized to resistivity values, are displayed in Table 1, along with DC measurements (see annex section A.1.1), finding a consistency in the results. The mean values and errors presented in Table 1 account for the measurements for the three different sample lengths. In this regard, the behavior

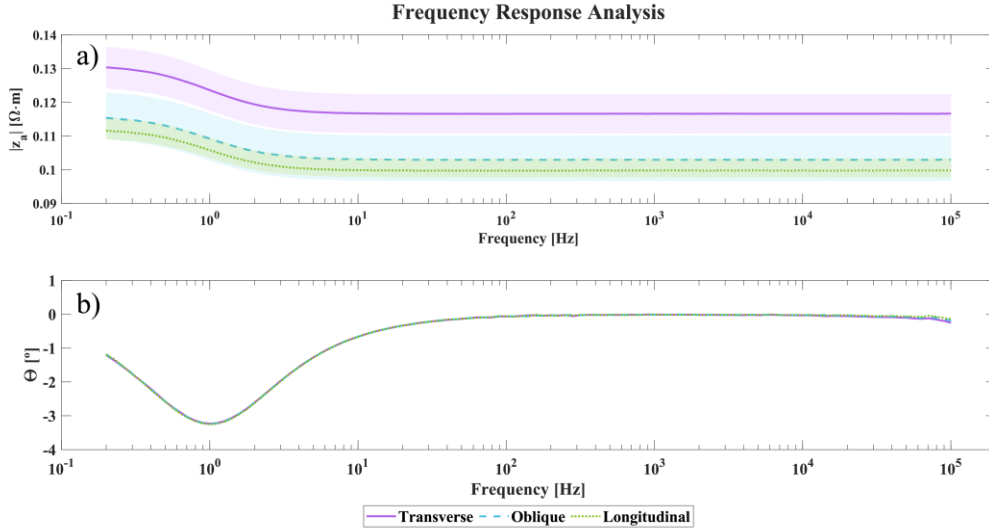of PLA/CB composites for power frequency ranges (50/60Hz) approaches to that measured under DC regime.

Figure 3: Experimental results of Frequency Response Analysis. a) Apparent impedivity modulus vs Frequency for [0.2Hz-0.1MHz] range. b) Phase angle vs Frequency for [0.2Hz-0.1MHz] range. Three samples of each printing direction type were used. The solid lines represent the averages of the three length responses, while the shade represents the maximum dispersion between these three.

Table 1: Apparent resistivity values for each signal type. The equivalent resistance of the FRA response between 40Hz and 0.1 MHz has been used to calculate variable frequency apparent resistivity.

Signal type	Apparent resistivity [Ω·m]		
	Transverse samples	Oblique samples	Longitudinal samples
Direct Current	0.115±0.004	0.102±0.005	0.098±0.003
Variable Frequency	0.116±0.006	0.103±0.007	0.099±0.003

The results collected in Table 1 show an agreement between both experimental characterization of resistivities. Thus, it is confirmed an enhancement in the electrical conductivity of 3D printed PLA/CB samples when the current flow direction approaches to 0º (longitudinal); whereas there is a reduction in conductivity when it approaches 90º (transverse). The voids formed during the printing process cause the obstruction of conductive paths formation. Thus, a higher void area in the cross-section perpendicular to the current flow causes a higher electrical resistivity, see Fig. 2c.

3.2 Thermo-electric behavior

This section presents the results obtained from the thermo-electrical characterization tests and their discussion. The temperature fields of different samples were obtained during the heating of the material caused by the flow of electric current. Whenever an electric current flows through a material, it gets heated due to an increase in its internal energy (i.e., Joule heating, Eq. (1)). This effect is extremely important when the voltage applied is sufficiently high, as the increase in material's temperature will impact both electrical and mechanical responses. The dissipated heat, Q_J, due to this effect can be expressed as a volume integral within the domain Ω as stated in Eq. (1).

$$Q_J = \int_0^t \int_\Omega \frac{V^2}{R} d\Omega \, dt \tag{1}$$

Where V is the voltage, t is the time and R is the electric resistance. The dispersion of conductive particles within the matrix and location of voids during printing lead to the heterogeneous formation of conductive paths. Therefore, it is expected that the circulation of the electric current in these printed materials will not necessarily present a uniform and homogeneous heating. In this section, we evaluate the interrelations between thermal and electric behaviors. Such an interplay is determined by analyzing the influence of various factors such as filament adhesion and micro voids or particles dispersion at the microscale.

When applying the DC voltage, the resistive behavior of the material results in heat generation leading to a temperature increase. Moreover, there is a bilateral coupling in which the temperature increase promotes a growth in the internal resistance, with a subsequent reduction in conducted current [39]. This current reduction decreases the heat generated with time until it is equal to the heat dissipated through convection and radiation, reaching thermal equilibrium. Thus, these PLA-based materials may help at limiting current consumption for certain electric loads, opening potential applications as a protective device. The conductive properties of the PLA conductive composite are given by the presence of CB particles, and hence the current will follow the paths created by the alignment of those particles. For this reason, it is expected to observe differences in Joule heating for different variables that may favor or hinder the particles-path generation. Therefore, the thermo-electric response of the material will highly depend on effects such as voids distribution or thermal dilatation of the matrix.

3.2.1 Resistive response and thermo-electric heat dissipation

To obtain the overall electric and thermal responses over time, two magnitudes were measured: the average temperature and the apparent resistivity of the whole sample. The results for 2L samples when subjected to 30V (electric field of 181 V/m), 60V (electric field of 375 V/m) and 90V (electric field of 545 V/m) are shown in Fig. 4. For more detailed information, please see the annex section, Figs. A3 to A5. For every printing orientation, the greatest increase in temperature and apparent resistivity happens during the first five minutes. When the temperature starts to increase due to the current flow, the apparent resistivity of the sample does too. This increase in the sample resistance leads to a decrease in heat generation according to Eq. (1). This process evolves until thermal and electrical equilibrium is reached, balancing internal heating with convection cooling. This stabilization appears in almost all the applied electric fields, except for electric fields that heat the material to temperatures higher than 110ºC, when the apparent resistivity starts to drastically decrease, dotted green and blue lines in Fig. 4. When the applied electric field heats the samples to a temperature below the glass transition, both resistance and temperature follow an increasing tendency at every point. This tendency can be observed below electric fields of 375 V/m, as 30V for 1L samples, 60V for 2L samples and below 80V for 2.75L samples; see Figs. A3-A5. Exceeding the glass transition temperature of composite, 62ºC (see Fig. 1), changes the electrical dependence of the composite with the temperature. At that point, the temperature maintains an increasing tendency, while the apparent resistivity reaches its highest value followed by a slow decrease until stabilization. Fig. 4 shows that both oblique and longitudinal samples exhibit similar electric and thermal responses except for the highest voltages. However, the response of transverse samples differs from their counterparts. This effect occurs with every length studied in this contribution. Irrespective of the electric field applied, transverse samples show a higher apparent resistivity than the oblique and longitudinal ones at every time step, as it can be seen in Fig. 4 and Figs. A3-A5. As expected from Eq. (1), an opposite trend is observed in its thermal response, where transverse samples reach inferior temperatures. Another important factor to consider is the stabilization time of the specimens. As presented in Fig. 4, the stabilization time does not depend drastically on the printing orientations, but on the voltage applied. This fact can also be seen in Figs. A4-A5, where the voltage that firstly reaches the glass transition temperature (i.e., 60V for 2L samples and 80V for 2.75L samples) takes the longest time to achieve the stabilization. Until this glass transition temperature voltage is applied, an increase in voltage associates an increase in the

stabilization time. Furthermore, once the glass transition temperature voltage is surpassed, an increase in the voltage leads to a decrease in the stabilization time.
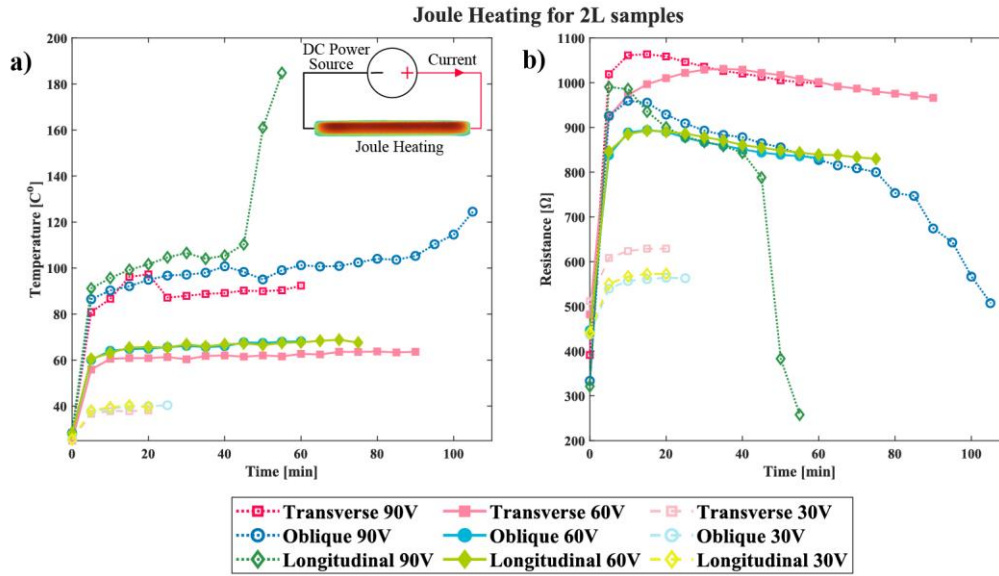

Figure 4: Experimental temperature and apparent resistivity results for 2L samples heated by Joule effect imposing three DC voltages: 30V (dashed lines), 60V (solid lines) and 90V (dotted lines). These results are presented for longitudinal, oblique and transverse samples. a) Average temperature is plotted against time. b) Electric apparent resistivity is plotted against time.

From the results presented in Fig. 4 and Figs A3-A5, it becomes clear that there are three types of electro-thermal stresses. The first ones are those which lead to a rise of apparent resistivity and temperature up to saturation values, maintaining temperatures below glass transition temperature. The second one is related to higher electrical stresses, where stabilization is reached for apparent resistivity and temperature, but the latter surpasses glass transition, which provokes a change in trend for apparent resistivity before stabilization. Finally, the third electrical stress level type is so high that the stabilization does not take place, and a destructive thermal runaway occurs.

Due to the inherent formation of voids during the FFF printing and their distribution depending on the printing orientation, the resistance of each sample is influenced by this parameter. The electrodes used to apply the DC voltage to PLA samples were placed so that the electric current preferably circulates along their longitudinal axis. Therefore, it seems logical that a filament deposition with an angle closer to this axis will improve the overall electric response, caused by the lower probability of finding voids along the filament (see Fig.2). Following Eq. (1), the generated heat is inversely proportional to the sample resistance, which explains the higher temperatures reached in longitudinal and oblique specimens due to their lower resistance. In addition, the electric apparent resistivity has a dependence on the temperature. Fig. 4 shows how the bilateral dependence of temperature and apparent resistivity determines the response below glass transition. Nevertheless, when glass transition temperature is surpassed, the polymeric chain mobility increases, thus favoring the movement of CB particles within the matrix. This improvement in mobility may enhance the alignment of particles and hence the creation of new conductive paths. For this reason, apparent resistivity-time curves of samples that have exceeded the glass transition temperature show a decrease in the apparent resistivity until the stabilization, see solid lines in Fig. 4. Moreover, thermal dilatation phenomenon can also affect the resistive response of the material when heated. A dilatation of the polymeric matrix due to thermal expansion [54] changes the distance between conductive particles, resulting in the breakages of conductive paths. Once the trigger temperature of 110ºC is surpassed a destabilization occurs, leading to a drastic increase in electrical conductivity and heating. This

trigger temperature coincides with the peak temperature of crystallization of the composite (see Fig. 1). Adding the improvement of polymeric chain mobility after glass transition with the rearranging of polymeric chains during crystallization leads to such a drastic increase in conductivity. Nevertheless, it seems complicated to predict precisely the time that this destabilization takes part, as well as the electric field needed to obtain that effect. For example, oblique 2.75L sample destabilizes at 120V (electric field of 528 V/m), differing from its counterparts, that destabilized at 110V (electric field of 484 V/m).

3.2.2 Influence of printing conditions on the thermo-electrical behavior

The results presented in the previous sections suggest certain dependences of the thermo-electrical behavior on printing conditions. In this regard, the coupled response is influenced by mesostructural aspects such as the bounding between filaments, the deposition orientation and the resulting void distributions. Local heterogeneities in the mesostructure are expected due to the inherent nature of the printing process. Therefore, local changes in the material resistivity are expected to be associated to these heterogeneities. As a consequence of the latter, heating due to Joule effect will lead to temperature gradients within the sample due to variations in local resistivity/conductivity. To delve into these aspects, we performed an analysis of the temperature profile along the longitudinal axis of the sample under the application of different voltages.

First, we provide a qualitative analysis. To this end, we present the temperature profile along the longitudinal axis depicting thermal gradients during Joule heating for 2L samples manufactured with different printing orientations. The voltages considered for this qualitative analysis were 60V and 90V. The 60V condition was chosen, as this is the voltage for which the 2L samples reach the material glass transition temperature. Moreover, the 90V condition was chosen because this is the voltage that induces thermo-electrical destabilization. The results for these temperature profiles over time are shown in Fig. 5. This representation allows the visualization of thermal gradients along the sample and if the overall stabilization in temperature occurs within the whole sample.
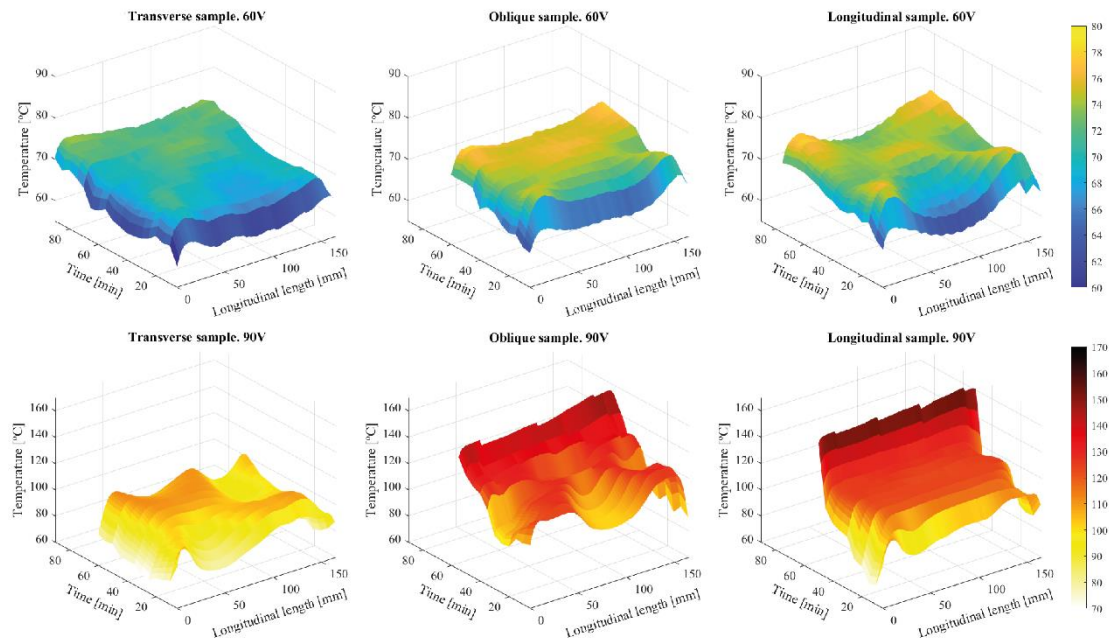

Figure 5: Experimental results of temperature variation along the central longitudinal axis of 2L samples through time. First row shows temperature variation for samples heated at 60V; second row shows temperature variation for samples heated at 90V.

As shown in Fig. 5, for a 60V heating, most heterogeneities appear in the longitudinal sample, followed by the oblique one and with the transverse sample as the one with more homogeneous behavior. Nevertheless, when the applied voltage increases up to 90V, the order of the samples with higher number of heterogeneities changes. In this case, the transverse sample presents the higher rate of heterogeneities throughout all the tests. The oblique sample exhibits a highly heterogeneous response during the first minutes of the experiment, when temperatures do not exceed 120ºC, and tends to stabilize its temperature profiles when values exceed 120ºC. Finally, the longitudinal sample presents highly homogeneous temperature profiles after the first 10 minutes, corresponding to temperature values above 120ºC.

We also provide quantitative analysis considering three repetitions per test condition to ensure repeatability, using virgin samples for every condition. In addition, tests applying 30V were added. For this analysis, we define a heterogeneity factor (ξ) to provide quantification of microstructural imperfections and their impact on the thermo-electrical response. This factor is defined as a dimensionless parameter that gathers the variations of temperature of each profile, following Eq. (2):

$$\xi = \frac{\sum_{j=1}^{N}\left(\dfrac{\sqrt{\dfrac{\sum_{i=1}^{n}\left(T_i^j-\bar{T}^j\right)^2}{(n-1)\cdot\bar{T}^j}}}{}\right)}{N} \tag{2}$$

where n represents the number of temperature values along the longitudinal axis at certain time, N represents the number of time measurements, T_i^j is the temperature value in the i spatial point at the time point j, and $\bar{T}^j$ is the average temperature at the time point j.

The results for the heterogeneity factor are shown in Table 2. Two main findings can be highlighted: i) generally, oblique samples exhibit more homogeneous heating than their counterparts, and ii) an increase in the electric potential augments heating heterogeneities. However, two cases deviate from this trend, both the oblique and the longitudinal heterogeneity factors at 90V, see Table 2. In both cases, heterogeneity factors are lower than the ones obtained for 60V, even though the voltage applied is higher. Furthermore, the longitudinal heterogeneity factor is lower than the oblique one, changing the tendency followed by previous voltages. These results match with the qualitative analysis displayed in Fig. 5.

Table 2: Heterogeneity factors (ξ) for three printing orientations and three applied voltages: 30V, 60V and 90V. Three samples of each printing orientation type were used.

Applied voltage (V)	Factor ξ (-) depending on the printing orientation		
	Transverse	Oblique	Longitudinal
30	0.0170±0.0011	0.0144±0.0026	0.0162±0.0019
60	0.0203±0.0054	0.0193±0.0029	0.0209±0.0061
90	0.0238±0.0024	0.0187±0.0028	0.0147±0.0015

In previous sections it was proven how the formation of conductive paths is easier for the longitudinal printing orientation, followed by the oblique one. It must be noted that the discussion in the previous sections mainly focused on conductive paths formed in the same longitudinal direction. However, electrons within the sample can also move in the transverse directions. This is an important point as the Joule heating is directly linked to the current flow irrespective of the flow direction. Thus, the formation of heating heterogeneities does not only depend on the general conductive path formation, but also on possible obstruction of those paths in any direction. Therefore, a clear relation between the sample resistance measured in the

previous sections and thermal heterogeneities is not obvious. In this regard, the results obtained at high applied voltages (e.g., 90V) are consistent with the overall samples' resistance. Moreover, for the oblique printing orientation, if one filament presents a failure, the probability of continuing the conductive path obstruction is lower as this is surrounded by two perpendicular filaments. This contributes to a better homogeneous behavior of these samples. Besides these microstructural aspects, it is important to remark how the softening of the matrix at temperatures above the glass transition allows the rearrangement of particles, changing the conductive paths during the heating. This effect is specially reflected in the longitudinal sample heated with 60V (Fig. 5), in which hot spots locations vary over time. Thermal dilatation can also have an important role in the evolution of heterogeneities, moving away particles in hot spots and increasing the resistance in that zone, thus leading to a decrease in Joule heating. In addition, it is important to highlight how for general destabilization temperatures (higher than 130ºC), the heterogeneity decreases, tending to behave as and homogeneous conductive material.

3.3 Thermo-electro-mechanical behavior

The use of conductive PLA structural components in devices subjected to both mechanical and electrical loads generates the need to study how each loading type impacts each other. Here, we approach this study from two perspectives. First, the mechanical response of the material was analyzed mimicking operational conditions. To do so, the thermal heating due to Joule effect expected when imposing operational voltage conditions was simulated by mechanically testing the samples in an environmental chamber. Then, we analyzed the possible alteration in mechanical properties after electrical load cycles.

3.3.1 Thermo-mechanical behavior under uniaxial tensile loading

When the composite is subjected to electric fields, temperature variations occur due to Joule heating. This change in temperature during an electrical operation of PLA conductive devices does not only change the electrical response of the material. Due to the thermoplastic nature of the matrix, if it reaches high enough temperatures, it will experience phase transitions significantly impacting the mechanical properties. Therefore, thermo-mechanical tests are needed to evaluate the effects of temperature in an isolated manner, to help the understanding of mechanical variations when applying electric currents in the material. The results of the thermo-mechanical tests conducted on the conductive material are presented in Fig. 6, split into printing orientation conditions. We also present in Fig. 6 the relation of Young's modulus and the maximum strain reached for each testing temperature.

Depending on the temperature of the experiment, different findings can be highlighted. At room temperature (25ºC), irrespective of the printing orientation, the material shows a brittle fracture at low strain values. When temperature increases up to 50ºC, the Young's modulus decreases. For oblique and longitudinal samples, the behavior of the material presents a transition from brittle to ductile, undergoing a small plastic strain hardening at strains higher than 0.1. While transverse samples do not reach yielding, they failed at a similar strain than for room temperature. For 80ºC, when the glass transition temperature of PLA/CB (62ºC) is surpassed, the stiffness drastically decreases and, for every printing orientation, the material behaves as ductile. When reaching 130ºC, some stiffness is recovered due to the cold crystallization of the PLA matrix [52], that according to Fig. 1 appears between 90-140ºC. This cold crystallization increases the stiffness of the material due to the generation of crystallized forms within the PLA matrix, specially at temperatures near 120ºC [52]. However, the maximum strain decreases to values near to the ones obtained at room temperature, being especially relevant for transverse samples. As an important remark, we note the influence of printing orientation on the failure strain and stress.

The thermo-mechanical response of this material presents a similar behavior for oblique and longitudinal samples, while transverse samples exhibit lower mechanical properties. These observations can be explained by the similarity of longitudinal and oblique voids geometry,

being in both cases triangular shapes, while transverse samples present rectangular voids in the cross section. A schematic representation of void distributions in each printing orientation is presented in Fig. 2. An incomplete filament adhesion process appears at the bottom corners of the filaments, creating triangular voids with 60 μm of height and 120 μm of width along the printing direction. Nevertheless, as the experiments performed induce tensile force along the longitudinal axis, the void geometry impacting the mechanical behavior is the cross-sectional one. For this case, only longitudinal samples maintain the mentioned dimensions, 60 μm of height and 120 μm of width. Oblique samples' voids maintain the triangular shape but increase their width up to 170 μm. Transverse voids, rather than maintaining a triangular shape, change to a rectangular one, with a width equal to the representative volume and a varying height (depending on the point where the cross section is chosen). In addition, the direction of the filament adhesion area is perpendicular to the printing direction, changing into a tendency to separate the filaments for a transverse sample, or breaking them for a longitudinal one.
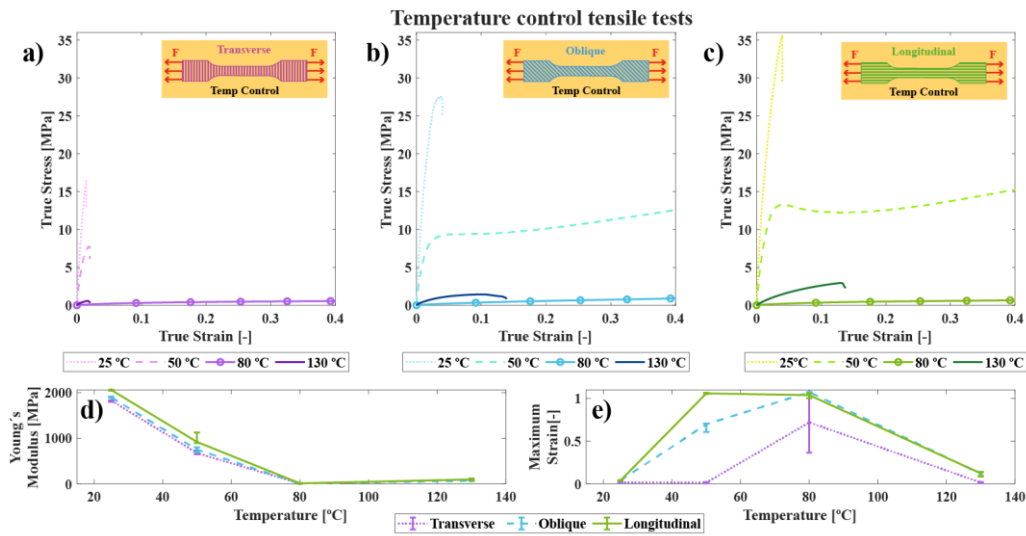

Figure 6: Experimental results of uniaxial tensile tests performed on 2L samples at fixed temperatures. a) True stress vs true strain curves for transverse printing orientation. b) True stress vs true strain curves for oblique printing orientation. c) True stress vs true strain curves for longitudinal printing orientation. d) Young's modulus of each printing orientation with respect to the experiment temperature. e) Maximum strain of each printing orientation with respect to the experiment temperature. Three samples for each printing orientation type were tested.

These microstructural features can explain the differences in the mechanical response of each sample type. As it can be seen in Fig. 6, the difference in maximum stress at room temperature for the longitudinal samples is more than two times higher than the one reached by transverse ones. However, the ratio between composite filled area (see ρ_T in Fig. 2c) is not lower than 0.5. This fact shows how the strength of filament adhesion is presumably weaker than the filament itself. For oblique samples, where the filament adhesion plane presents a 45º angle with respect to the tensile load, a weaker behavior is also reflected in the results of Fig. 6.

When the temperature increases up to 50ºC, the polymeric matrix softens resulting in a decrease in its Young's modulus proportionally for every printing direction. At this temperature, transverse samples still exhibit fracture under low strains, while oblique and longitudinal samples' response changes to a high strain plasticity, reaching deformation values up to 100%. This clear change in failure shows how bonding between filaments reduces the strength at temperatures below the glass transition. This effect can also be seen in the oblique samples, obtaining a considerably inferior maximum strain than their longitudinal counterparts. When surpassing the glass transition temperature of PLA, an extreme softening of the matrix appears, greatly decreasing the Young's modulus for every printing orientation. The sintered area

behavior starts approaching to the filament's one, getting a similar stress-strain response for every printing direction. Nevertheless, the filament adhesion surface still seems weaker than the filament area by its own, on account of the early failure of some transverse samples while comparing with longitudinal or oblique one. When reaching 130ºC, the sintered area returns to have a much weaker behavior than the filament, as it is reflected on the premature failure of transverse samples in Fig. 6. At this temperature, the main fracture mechanism is based on the separation of filaments, except for the longitudinal specimens, where no stress tends to separate them.

3.3.2 Mechanical behavior after thermo-electrical aging

A mesostructural analysis of thermo-electrically aged longitudinal samples is presented in Fig. 7. We provide a SEM image for every heating cycle voltage: a) virgin sample; b) heated with 30V; c) heated with 60V; d) heated with 90V. See Table 4 for more information about the time exposure to electrical loads and maximum temperature reached for every voltage. The porosity and mean void area values after each aging are presented in Table 3. Note that there is a great increase in voids area and porosity for samples heated with 90V, which results in subsequent thermo-electrical destabilization (see section 3.3.1). Those samples were disconnected from the power source after surpassing 210ºC, a temperature 60ºC higher than PLA/CB melting point. At such higher temperatures the inner voids dilate [55], as the composite stiffness at this temperature is not high enough to support the pressure of the air captured in those voids.
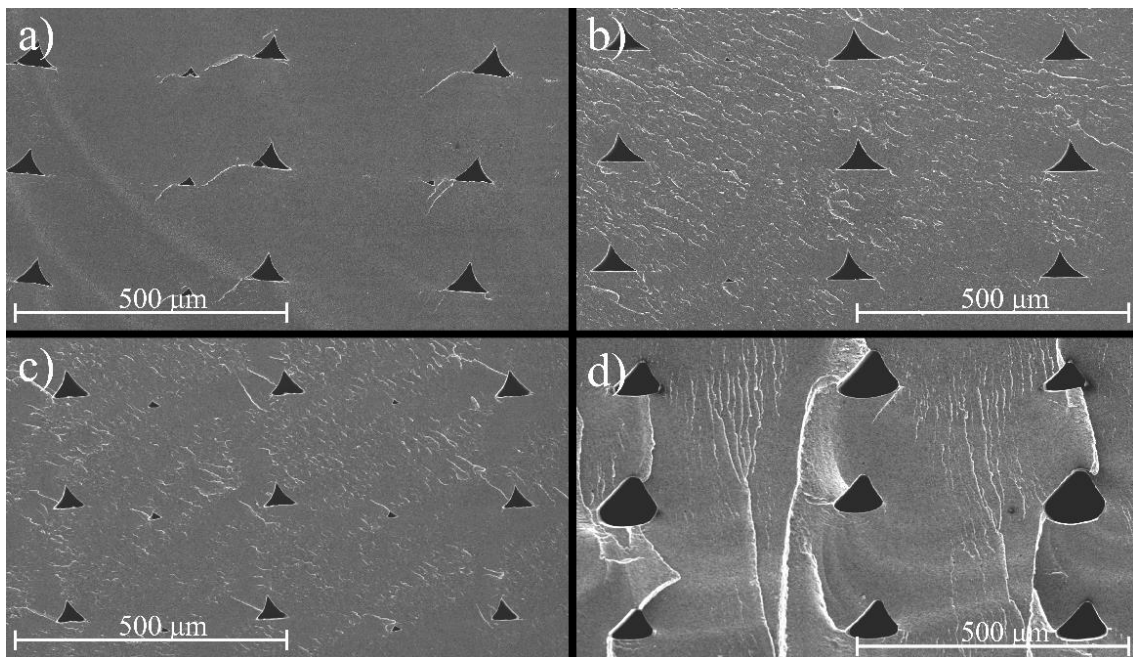

Figure 7: SEM images of the mesostructure of longitudinal 2L samples after being heated by Joule effect. a) Virgin sample; b) heated with 30V (E=181 V/m); c) heated with 60V (E=375 V/m); d) heated with 90V (E=545 V/m).

Table 3: Porosity and mean void area after thermo-electrical aging for 2L samples.

Parameter	Heating Voltage			
	0V	30V	60V	90V
Porosity [%]	1.44	2.15	1.42	13.44
Mean void area [μm^2]	659	671	637	3928

We present the results on the mechanical properties of the material after electric cycle application with a subsequent heating cycle. These results are shown in Fig. 8, split into stress-strain curves for every printing orientation. We additionally present the Young's modulus values and maximum strain reached for every voltage applied. For every printing orientation, two clear tendencies can be appreciated. First, the increase in applied voltage (i.e., increase in heating) decreases the failure strain, with an exception for samples heated with 90V. Second, when increasing the voltage, the stiffness of the aged samples increases except for samples heated with 90V. With respect to failure stress, there are no clear dependencies with the voltage applied, except again for 90V heating, that shows a weaker nature. The change in stress tendencies found in 90V can be explained by the drastic variation in voids size after thermo-electrical destabilization. In those cases, the effective area supporting the load is considerably decreased
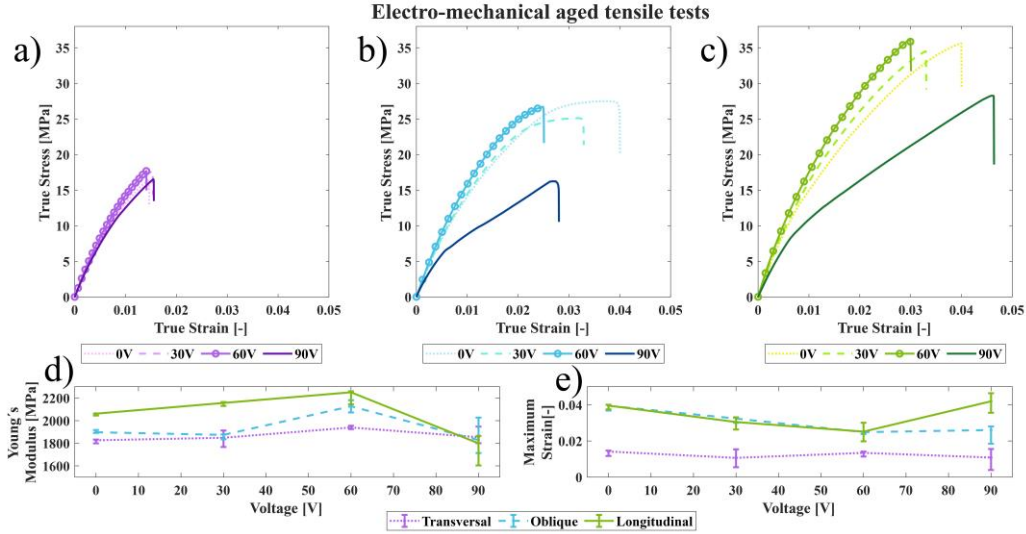

Figure 8: Experimental results of uniaxial tensile tests performed on 2L samples electro-mechanical aged at different voltages. a) True stress vs true strain curves for transverse printing orientation. b) True stress vs true strain curves for oblique printing orientation. c) True stress vs true strain curves for longitudinal printing orientation d) Young's modulus of each printing orientation with respect to the aging voltage. e) Maximum strain of each printing orientation with respect to the aging voltage. Three samples for each printing orientation type were tested.

Table 4: Maximum reached temperature during thermos-electrical aging, time exposure to electrical current during thermos-electrical aging. Three samples of each printing direction were used to obtain the mean values as well as the standard deviation, making a total of nine samples per shown result.

Parameter	Heating Voltage			
	0V	30V	60V	90V
Maximum reached temperature[℃]	-	48.1±0.9	78.7±3.9	210.0±0.0
Time exposure [min]	-	25.0±0.0	57.5±2.5	15.0±5.0

It is important to remark the influence of the sintered area in these changes in mechanical properties that, as in the thermo-mechanical behavior, is a crucial factor to predict the final mechanical performance. Nevertheless, sintered area weakening does not have such a big dependence with thermo-electrical aging as it has with the increase in temperature. This is reflected in the slight variations in stiffness and failure strain of transverse samples. In contrast, when the tensile load is supported by the filament instead of the sintered area, the changes in behavior are accentuated (see oblique and longitudinal curves of Young's Modulus and maximum strain of Fig. 8). These results stand transverse printed components as more reliable for devices with varying voltage, showing a very similar response independently of the heating cycle.

4. Conclusions

This work provides experimental evidence on the mechanical degradation of a 3D printed conductive PLA/CB composite due to the application of electric fields. Prior to this analysis, a comprehensive thermo-electro-mechanical characterization of the material improves the understanding of its response under in service electro-mechanical work regimes. Due to the inherent anisotropy of the FFF printing process, void location and orientation have a significant impact on the material performance. The electrical and thermo-electrical responses are independent with the length, discarding non-desirable effects due to the accumulation of printing errors. The printing orientation was found as the main parameter dominating those responses, determining the direction of the mesostructural voids formed during samples manufacturing. This voids direction has been proved to highly influence the formation of conductive paths within the samples. Thus, the electrical conductivity of the samples is enhanced when the direction of the current flow is parallel to the printing orientation. Due to the coupled response between thermal and electrical behaviors, the heating of the samples is also affected by the printing orientation, reaching higher temperatures in samples with higher conductivity. The mechanical behavior of PLA/CB composite has been proved to be highly dependent on temperature. Significant changes in stiffness and ductility appear when the different phases of the polymer are transitioned. In this regard, glass transition and cold crystallization temperatures have been identified as thresholds which define mechanical and thermo-electrical behavior. These phase transitions within the polymeric matrix are identified as the main player in material degradation due to thermo-electric loading, changing the mechanical behavior by inducing an increase in mesostructural pore size.

Although this work provides new insights into the multifunctional response of conductive thermoplastics, further efforts are needed to unravel the microstructural dynamics of the conductive particles during and after electric actuation. In this regard, future work must consider different polymeric matrices to evaluate the stiffness influence and viscoelastic dependence. The development of new microstructural-based computational models will also help to this understanding. Overall, the detailed understanding of the thermo-electro-mechanical response of

PLA/CB composite through this experimental study, particularly its links with the printing orientations, will facilitate the use of this emerging material in devices subjected to domestic power ranges. Moreover, the thermo-electro-mechanical degradation analysis over time will help users in addressing the reliability concerns at the time a sensor device needs.

CRediT authorship contribution statement

J. Crespo-Miguel: Investigation, Data curation, Experimental methodology, Formal analysis, Writing-original draft, Writing-review & editing. **D. Garcia-Gonzalez:** Conceptualization, Investigation, Formal analysis, Writing-original draft, Writing-review & editing. **G. Robles:** Investigation, Formal analysis, Writing – review & editing. **M. Hossain:** Formal analysis, Writing – review & editing. **J.M. Martinez-Tarifa:** Conceptualization, Investigation, Experimental methodology, Formal analysis, Writing-review & editing, Funding acquisition. **A. Arias:** Conceptualization, Investigation, Formal analysis, Writing-review & editing, Funding acquisition.

References

[1]	J. C. Tan and H. Y. Low, "Multi-materials fused filament printing with embedded highly conductive suspended structures for compressive sensing," Addit Manuf, vol. 36, p. 101551, Dec. 2020, doi: 10.1016/J.ADDMA.2020.101551.

[2]	M. Borghetti, M. Serpelloni, and E. Sardini, "Printed Strain Gauge on 3D and Low-Melting Point Plastic Surface by Aerosol Jet Printing and Photonic Curing," Sensors, vol. 19, no. 19, p. 4220, Sep. 2019, doi: 10.3390/s19194220.

[3]	S. J. Leigh, R. J. Bradley, C. P. Purssell, D. R. Billson, and D. A. Hutchins, "A Simple, Low-Cost Conductive Composite Material for 3D Printing of Electronic Sensors," PLoS One, vol. 7, no. 11, p. e49365, Nov. 2012, doi: 10.1371/journal.pone.0049365.

[4]	N. Lazarus and S. S. Bedair, "Creating 3D printed sensor systems with conductive composites," Smart Mater Struct, vol. 30, no. 1, p. 015020, Jan. 2021, doi: 10.1088/1361-665X/abcbe2.

[5]	J. Lee, M. O. Faruk Emon, M. Vatani, and J.-W. Choi, "Effect of degree of crosslinking and polymerization of 3D printable polymer/ionic liquid composites on performance of stretchable piezoresistive sensors," Smart Mater Struct, vol. 26, no. 3, p. 035043, Mar. 2017, doi: 10.1088/1361-665X/aa5c70.

[6]	J. G. Jeon, G.-W. Hong, H.-G. Park, S. K. Lee, J.-H. Kim, and T. J. Kang, "Resistance Temperature Detectors Fabricated via Dual Fused Deposition Modeling of Polylactic Acid and Polylactic Acid/Carbon Black Composites," Sensors, vol. 21, no. 5, p. 1560, Feb. 2021, doi: 10.3390/s21051560.

[7]	M. Nankali, N. M. Nouri, N. G. Malek, and M. Amjadi, "Dynamic thermoelectromechanical characterization of carbon nanotube nanocomposite strain sensors," Sens Actuators A Phys, vol. 332, p. 113122, Dec. 2021, doi: 10.1016/J.SNA.2021.113122.

[8]	S. Kim et al., "Wearable, Ultrawide-Range, and Bending-Insensitive Pressure Sensor Based on Carbon Nanotube Network-Coated Porous Elastomer Sponges for Human Interface

and Healthcare Devices," ACS Appl. Mater. Interfaces, vol. 11, p. 2022, 2019, doi: 10.1021/acsami.9b07636.

[9]   Y. S. Lui, W. T. Sow, L. P. Tan, Y. Wu, Y. Lai, and H. Li, "4D printing and stimuli-responsive materials in biomedical aspects," Acta Biomater, vol. 92, pp. 19–36, Jul. 2019, doi: 10.1016/J.ACTBIO.2019.05.005.

[10]   R. Balint, N. J. Cassidy, and S. H. Cartmell, "Conductive polymers: Towards a smart biomaterial for tissue engineering," Acta Biomater, vol. 10, no. 6, pp. 2341–2353, Jun. 2014, doi: 10.1016/J.ACTBIO.2014.02.015.

[11]   F. Fu, J. Wang, H. Zeng, and J. Yu, "Functional Conductive Hydrogels for Bioelectronics," ACS Mater Lett, vol. 2, no. 10, pp. 1287–1301, Aug. 2020, doi: 10.1021/acsmaterialslett.0c00309.

[12]   J. Zhou and S. Vijayavenkataraman, "3D-printable conductive materials for tissue engineering and biomedical applications," Bioprinting, vol. 24, p. e00166, Dec. 2021, doi: 10.1016/J.BPRINT.2021.E00166.

[13]   Y. Zhong, R. An, H. Ma, and C. Wang, "Low-temperature-solderable intermetallic nanoparticles for 3D printable flexible electronics," Acta Mater, vol. 162, pp. 163–175, Jan. 2019, doi: 10.1016/J.ACTAMAT.2018.09.069.

[14]   M. Luisa Lopez-Donaire et al., "2201707 (1 of 12) Computationally Guided DIW Technology to Enable Robust Printing of Inks with Evolving Rheological Properties," 2022, doi: 10.1002/admt.202201707.

[15]   I. Oh, Z. Zhu, H. E. Naguib, A. Jo, and C. Huet, "Template-Assisted Self-Assembly of Conductive Polymer Electrodes for Ionic Electroactive Polymers," 2020, doi: 10.3389/fbioe.2020.00837.

[16]   D. D. L. Chung, "Materials for electromagnetic interference shielding," Mater Chem Phys, vol. 255, p. 123587, Nov. 2020, doi: 10.1016/J.MATCHEMPHYS.2020.123587.

[17]   M. Rahaman, · Prashant Gupta, · Mokarram Hossain, · Ali Aldalbahi, A. Aldalbahi, and M. Rahaman, "Predicting Percolation Threshold Value of EMI SE for Conducting Polymer Composite Systems Through Different Sigmoidal Models," J Electron Mater, doi: 10.1007/s11664-022-09444-7.

[18]   R. Holze and Y. P. Wu, "Intrinsically conducting polymers in electrochemical energy technology: Trends and progress," Electrochim Acta, vol. 122, pp. 93–107, Mar. 2014, doi: 10.1016/J.ELECTACTA.2013.08.100.

[19]   Y. Qian, C. Li, Y. Qi, and J. Zhong, "3D printing of graphene oxide composites with well controlled alignment," Carbon N Y, vol. 171, pp. 777–784, Jan. 2021, doi: 10.1016/J.CARBON.2020.08.077.

[20]   O. Kaynan, A. Yıldız, Y. E. Bozkurt, E. Ozden Yenigun, and H. Cebeci, "Electrically conductive high-performance thermoplastic filaments for fused filament fabrication," Compos Struct, vol. 237, p. 111930, Apr. 2020, doi: 10.1016/J.COMPSTRUCT.2020.111930.

[21]   K. Gnanasekaran et al., "3D printing of CNT- and graphene-based conductive polymer nanocomposites by fused deposition modeling," Appl Mater Today, vol. 9, pp. 21–28, Dec. 2017, doi: 10.1016/J.APMT.2017.04.003.

[22]   A. Dorigato, V. Moretti, S. Dul, S. H. Unterberger, and A. Pegoretti, "Electrically conductive nanocomposites for fused deposition modelling," Synth Met, vol. 226, pp. 7–14, Apr. 2017, doi: 10.1016/J.SYNTHMET.2017.01.009.

[23]   Z. Lei et al., "Novel electrically conductive composite filaments based on Ag/saturated polyester/polyvinyl butyral for 3D-printing circuits," Compos Sci Technol, vol. 180, pp. 44–50, Aug. 2019, doi: 10.1016/J.COMPSCITECH.2019.05.003.

[24]   T. Wu and B. Chen, "Facile Fabrication of Porous Conductive Thermoplastic Polyurethane Nanocomposite Films via Solution Casting OPEN", doi: 10.1038/s41598-017-17647-w.

[25]   J. F. Feller, "Conductive Polymer Composites: Influence of Extrusion Conditions on Positive Temperature Coefficient Effect of Poly(butylene terephthalate)/Poly(olefin)–Carbon Black Blends," J Appl Polym Sci, vol. 91, pp. 2151–2157, 2004.

[26]   K. Dong, M. Panahi-Sarmad, Z. Cui, X. Huang, and X. Xiao, "Electro-induced shape memory effect of 4D printed auxetic composite using PLA/TPU/CNT filament embedded synergistically with continuous carbon fiber: A theoretical & experimental analysis," Compos B Eng, vol. 220, p. 108994, Sep. 2021, doi: 10.1016/J.COMPOSITESB.2021.108994.

[27]   A. Abdalla, H. H. Hamzah, O. Keattch, D. Covill, and B. A. Patel, "Augmentation of conductive pathways in carbon black/PLA 3D-printed electrodes achieved through varying printing parameters," Electrochim Acta, vol. 354, p. 136618, Sep. 2020, doi: 10.1016/J.ELECTACTA.2020.136618.

[28]   O. Sai Saran, A. Prudhvidhar Reddy, L. Chaturya, and M. Pavan Kumar, "3D printing of composite materials: A short review," Mater Today Proc, May 2022, doi: 10.1016/J.MATPR.2022.05.144.

[29]   J. R. C. Dizon, A. H. Espera, Q. Chen, and R. C. Advincula, "Mechanical characterization of 3D-printed polymers," Addit Manuf, vol. 20, pp. 44–67, Mar. 2018, doi: 10.1016/J.ADDMA.2017.12.002.

[30]   A. García-Collado, J. M. Blanco, M. K. Gupta, and R. Dorado-Vicente, "Advances in polymers based Multi-Material Additive-Manufacturing Techniques: State-of-art review on properties and applications," Addit Manuf, vol. 50, p. 102577, Feb. 2022, doi: 10.1016/J.ADDMA.2021.102577.

[31]   G. C. Psarras, "Hopping conductivity in polymer matrix–metal particles composites," Compos Part A Appl Sci Manuf, vol. 37, no. 10, pp. 1545–1553, Oct. 2006, doi: 10.1016/J.COMPOSITESA.2005.11.004.

[32]   K. Niendorf and B. Raeymaekers, "Combining ultrasound directed self-assembly and stereolithography to fabricate engineered polymer matrix composite materials with anisotropic electrical conductivity," Compos B Eng, vol. 223, p. 109096, Oct. 2021, doi: 10.1016/J.COMPOSITESB.2021.109096.

[33]   W. Wang and A. H. Jayatissa, "Computational and experimental study of electrical conductivity of graphene/poly(methyl methacrylate) nanocomposite using Monte Carlo method and percolation theory," Synth Met, vol. 204, pp. 141–147, Jun. 2015, doi: 10.1016/J.SYNTHMET.2015.03.022.

[34]   Y. P. Mamunya, V. v. Davydenko, P. Pissis, and E. v. Lebedev, "Electrical and thermal conductivity of polymers filled with metal powders," Eur Polym J, vol. 38, no. 9, pp. 1887–1897, Sep. 2002, doi: 10.1016/S0014-3057(02)00064-2.

[35]   M. Ba, Z. Zhang, and Y. Qi, "The Dispersion Tolerance of Micro/Nano Particle in Polydimethylsiloxane and Its Influence on the Properties of Fouling Release Coatings Based on Polydimethylsiloxane," Coatings, vol. 7, no. 7, p. 107, Jul. 2017, doi: 10.3390/coatings7070107.

[36]   S. Garzon-Hernandez, A. Arias, and D. Garcia-Gonzalez, "A continuum constitutive model for FDM 3D printed thermoplastics," Compos B Eng, vol. 201, p. 108373, Nov. 2020, doi: 10.1016/J.COMPOSITESB.2020.108373.

[37]   Y. Hara, K. Yoshida, A. Khosla, M. Kawakami, K. Hosoda, and H. Furukawa, "Very Wide Sensing Range and Hysteresis Behaviors of Tactile Sensor Developed by Embedding Soft Ionic Gels in Soft Silicone Elastomers," ECS Journal of Solid State Science and Technology, vol. 9, no. 6, p. 061024, Jan. 2020, doi: 10.1149/2162-8777/aba913.

[38]   S. Garzon-Hernandez, D. Garcia-Gonzalez, A. Jérusalem, and A. Arias, "Design of FDM 3D printed polymers: An experimental-modelling methodology for the prediction of mechanical properties," Mater Des, vol. 188, p. 108414, Mar. 2020, doi: 10.1016/J.MATDES.2019.108414.

[39]   I. Tirado-Garcia et al., "Conductive 3D printed PLA composites: On the interplay of mechanical, electrical and thermal behaviors," Compos Struct, vol. 265, p. 113744, Jun. 2021, doi: 10.1016/J.COMPSTRUCT.2021.113744.

[40]   L. P. Muthe, K. Pickering, and C. Gauss, "A Review of 3D/4D Printing of Poly-Lactic Acid Composites with Bio-Derived Reinforcements," Composites Part C: Open Access, vol. 8, p. 100271, Aug. 2022, doi: 10.1016/J.JCOMC.2022.100271.

[41]   A. Cano-Vicent et al., "Fused deposition modelling: Current status, methodology, applications and future prospects," Addit Manuf, vol. 47, p. 102378, Nov. 2021, doi: 10.1016/J.ADDMA.2021.102378.

[42]   L. Lei, J. Qiu, and E. Sakai, "Preparing conductive poly(lactic acid) (PLA) with poly(methyl methacrylate) (PMMA) functionalized graphene (PFG) by admicellar polymerization," Chemical Engineering Journal, vol. 209, pp. 20–27, Oct. 2012, doi: 10.1016/J.CEJ.2012.07.114.

[43]   N. M. Nordin, Y. F. Buys, H. Anuar, M. H. Ani, and M. M. Pang, "Development of Conductive Polymer Composites from PLA/TPU Blends Filled with Graphene Nanoplatelets," Mater Today Proc, vol. 17, pp. 500–507, Jan. 2019, doi: 10.1016/J.MATPR.2019.06.328.

[44]   G. Postiglione, G. Natale, G. Griffini, M. Levi, and S. Turri, "Conductive 3D microstructures by direct 3D printing of polymer/carbon nanotube nanocomposites via liquid deposition modeling," Compos Part A Appl Sci Manuf, vol. 76, pp. 110–114, Sep. 2015, doi: 10.1016/J.COMPOSITESA.2015.05.014.

[45]   M. Kim et al., "Characterization of resistive heating and thermoelectric behavior of discontinuous carbon fiber-epoxy composites," Compos B Eng, vol. 90, pp. 37–44, Apr. 2016, doi: 10.1016/J.COMPOSITESB.2015.11.037.

[46]   H. Kim and S. Lee, "Characterization of Electrical Heating of Graphene/PLA Honeycomb Structure Composite Manufactured by CFDM 3D Printer", doi: 10.1186/s40691-020-0204-2.

[47]   R. Taherian and Z. Samiei, "Investigation on electrical properties of polyvinyl acetate/graphite adhesive by joule heating and hall effect tests," Mater Today Commun, vol. 26, p. 101680, Mar. 2021, doi: 10.1016/J.MTCOMM.2020.101680.

[48]   J. Beniak, Ľ. Šooš, P. Križan, M. Matúš, and V. Ruprich, "Resistance and Strength of Conductive PLA Processed by FDM Additive Manufacturing," Polymers (Basel), vol. 14, no. 4, p. 678, Feb. 2022, doi: 10.3390/polym14040678.

[49]   A. Koterwa et al., "The role of electrolysis and enzymatic hydrolysis treatment in the enhancement of the electrochemical properties of 3D-printed carbon black/poly(lactic acid) structures," Appl Surf Sci, vol. 574, p. 151587, Feb. 2022, doi: 10.1016/J.APSUSC.2021.151587.

[50]   E. Vaněčková et al., "3D printed polylactic acid/carbon black electrodes with nearly ideal electrochemical behavior," Journal of Electroanalytical Chemistry, vol. 857, p. 113745, Jan. 2020, doi: 10.1016/J.JELECHEM.2019.113745.

[51]   P. F. Flowers, C. Reyes, S. Ye, M. J. Kim, and B. J. Wiley, "3D printing electronic components and circuits with conductive thermoplastic filament," Addit Manuf, vol. 18, pp. 156–163, Dec. 2017, doi: 10.1016/J.ADDMA.2017.10.002.

[52]   Chengbo Zhou et al., "Thermal strain-induced cold crystallization of amorphous poly(lactic acid)," CrystEngComm, vol. 18, no. 3237, 2016.

[53]   K. Wasanasuk and K. Tashiro, "Structural Regularization in the Crystallization Process from the Glass or Melt of Poly(L-lactic Acid) Viewed from the Temperature-Dependent and Time-Resolved Measurements of FTIR and Wide-Angle/Small-Angle X-ray Scatterings," vol. 44, pp. 9650–9660, 2011, doi: 10.1021/ma2017666.

[54]   R. Stopforth, "Conductive polylactic acid filaments for 3D printed sensors: Experimental electrical and thermal characterization," Sci Afr, vol. 14, p. e01040, Nov. 2021, doi: 10.1016/J.SCIAF.2021.E01040.

[55]   H. Švajdlenková, O. Šauša, I. Mat´ko, T. Koch, and C. Gorsche, "Investigating the Free-Volume Characteristics of Regulated Dimethacrylate Networks Below and Above Glass Transition Temperature," 2018, doi: 10.1002/macp.201800119.

Appendix

A.1 Validation

In this section electrical and thermo-electrical results regarding sample length are presented. By this, the independence of electric and thermo-electric response with length is studied. Thus, raster angle is found as the printing parameter that dominates the different responses and couplings in this material.

A.1.1 Independence of apparent resistivity with sample length

The electric resistance of a homogeneous specimen has a direct dependency with the resistivity of the material and geometrical features as is stated in Eq. (A.1).

$$R_o = \frac{\rho_o L}{A} \tag{A.1}$$

Where ρ_o is the resistivity of the sample, A is the cross section and L is its length. But when considering printed samples, the voids location does not allow the use of materials resistivity for a correct resistance calculation. Instead, an apparent resistivity will be used, regarding the effects of voids location in the normalization of resistance with length and area.

Both resistance and apparent resistivity results are shown in Fig. A1. Resistance values tend to increase accordingly with length, obtaining values twice higher for 2L than 1L samples; and 2.75 times higher for 2.75L than 1L samples. Using Eq. (A.1), but changing material resistivity by apparent resistivity, the results were expressed by means of the last one, see Fig. A1.

For every printing direction, the apparent resistivity presents similar values irrespective of the sample length: longitudinal samples exhibit apparent resistivity values of 0.098±0.003 Ω·m; oblique samples exhibit apparent resistivity values of 0.102±0.005 Ω·m; and transverse samples exhibit apparent resistivity values of 0.115±0.004 Ω·m. Transverse resistivity results are similar to the ones presented in the literature: 0.17 Ω·m [49] and 0.12 Ω·m [27]. The non-perfect match with literature resistivities can be caused by the difference in printing parameters and conditions.
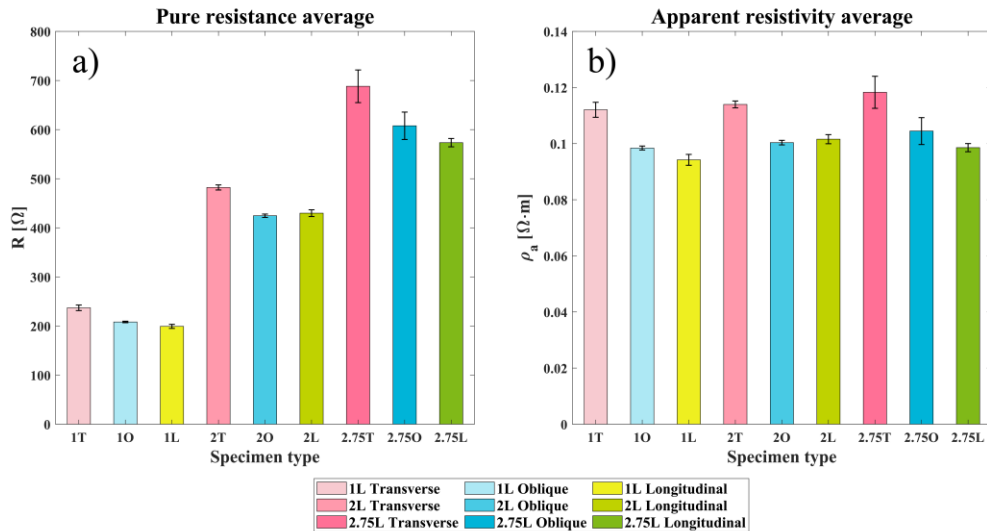

Figure A1: a) Experimental measurement of pure electric resistance for three printing orientations and three sample lengths. b) Experimental results of apparent resistivity for three printing orientations and three sample lengths. The printing orientations considered: transverse (pink), oblique (blue) and longitudinal (green). The sample length considered: 1L (82.5mm), 2L

(165mm) and 2.75L (227 mm). The error bars represent the standard deviation of the measurements. Five samples for each printing type were tested.

These results exhibit how the apparent resistivity of the samples does not depend on the length, but only on the printing orientation. Based on these findings, apparent resistivity will be used in the rest of the work, analyzing every resistive response in a normalized fashion.

A.1.2 Independence of Joule heating with sample length

The use of the same cross-section for each length-type sample allows the possibility of studying the heating variations irrespectively from their length.

To study the independence of the temperature change with length, temperature-time curves of different length samples, heated by Joule effect, were compared. To be able to correlate samples with different lengths, the ratio between the voltage applied and sample length must be the same, leading to an equal electric field. The comparisons for each printing orientation for a voltage ratio of 30V/1L (electric field of 363 V/m) are presented in Fig. A2. Each solid line represents the average temperature of the whole sample, while the shaded area represents the experimental dispersion. In Fig. A2 and Figs. A6-A8, the electro-thermal behavior of PLA/CB composite was found similar for samples with the same voltage-length ratio. These results suggest that the total amount of voids in the sample does not change the overall response, but the density of voids does. These results demonstrate that not only the initial apparent resistivity is independent of the sample length, but also the electro-thermal response.
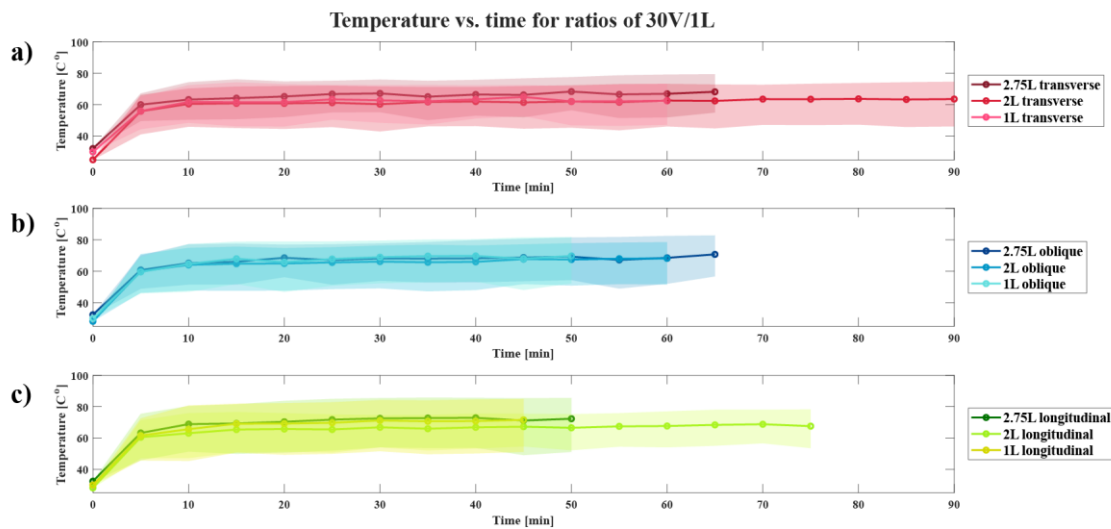

Figure A2: Experimental temperature results for samples with a constant voltage-length ratio of 30V/1L: a) transverse samples; b) oblique samples; and c) longitudinal samples. Solid line represents the mean temperature of each sample over time, while shaded area represents the experimental dispersion.
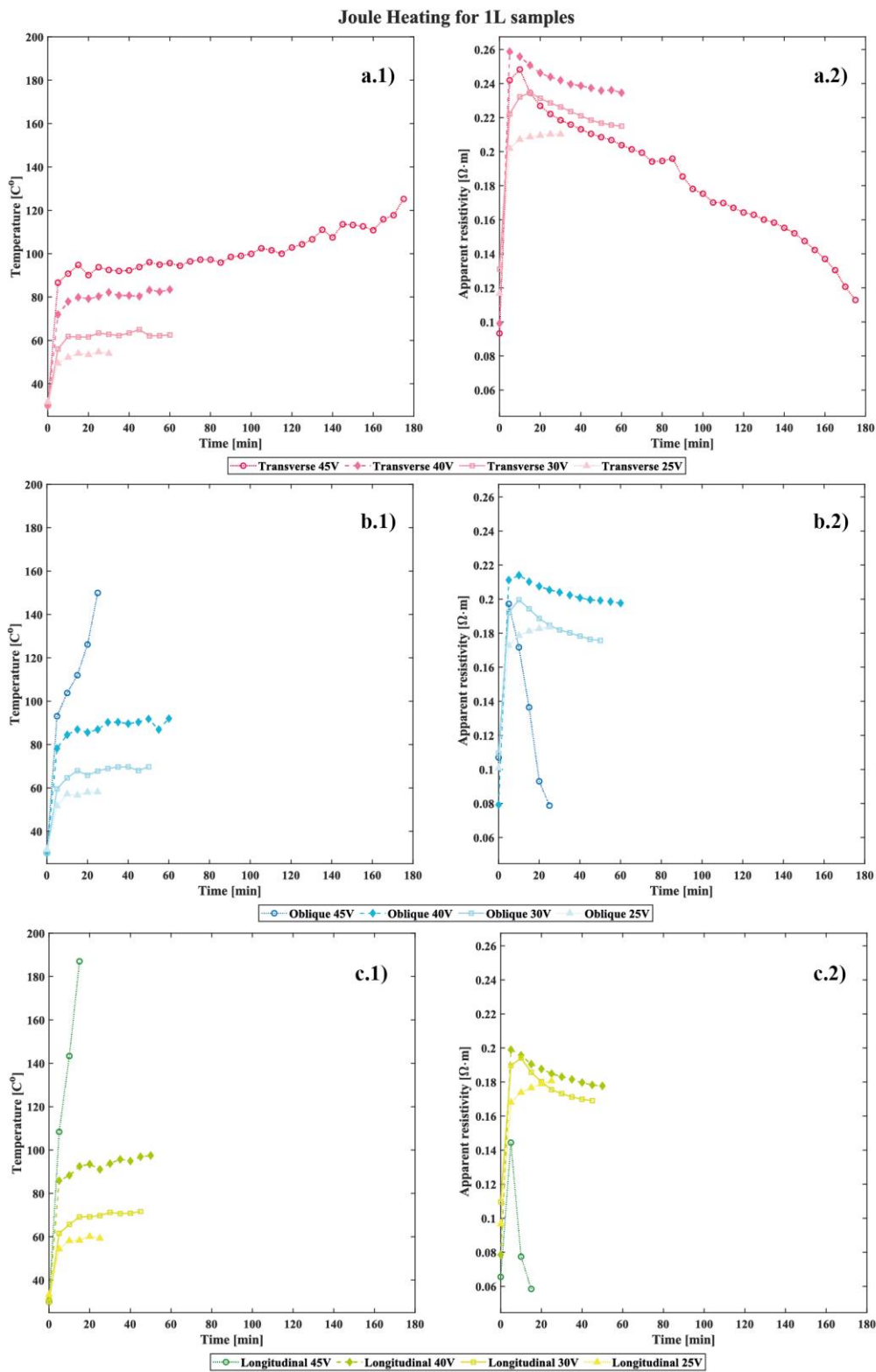
A.2 Additional figures

Figure A3: Experimental temperature and resistance results for 1L samples heated by Joule effect imposing four DC voltages from 25V to 45V. a) Transverse samples, b) oblique samples and c) longitudinal samples
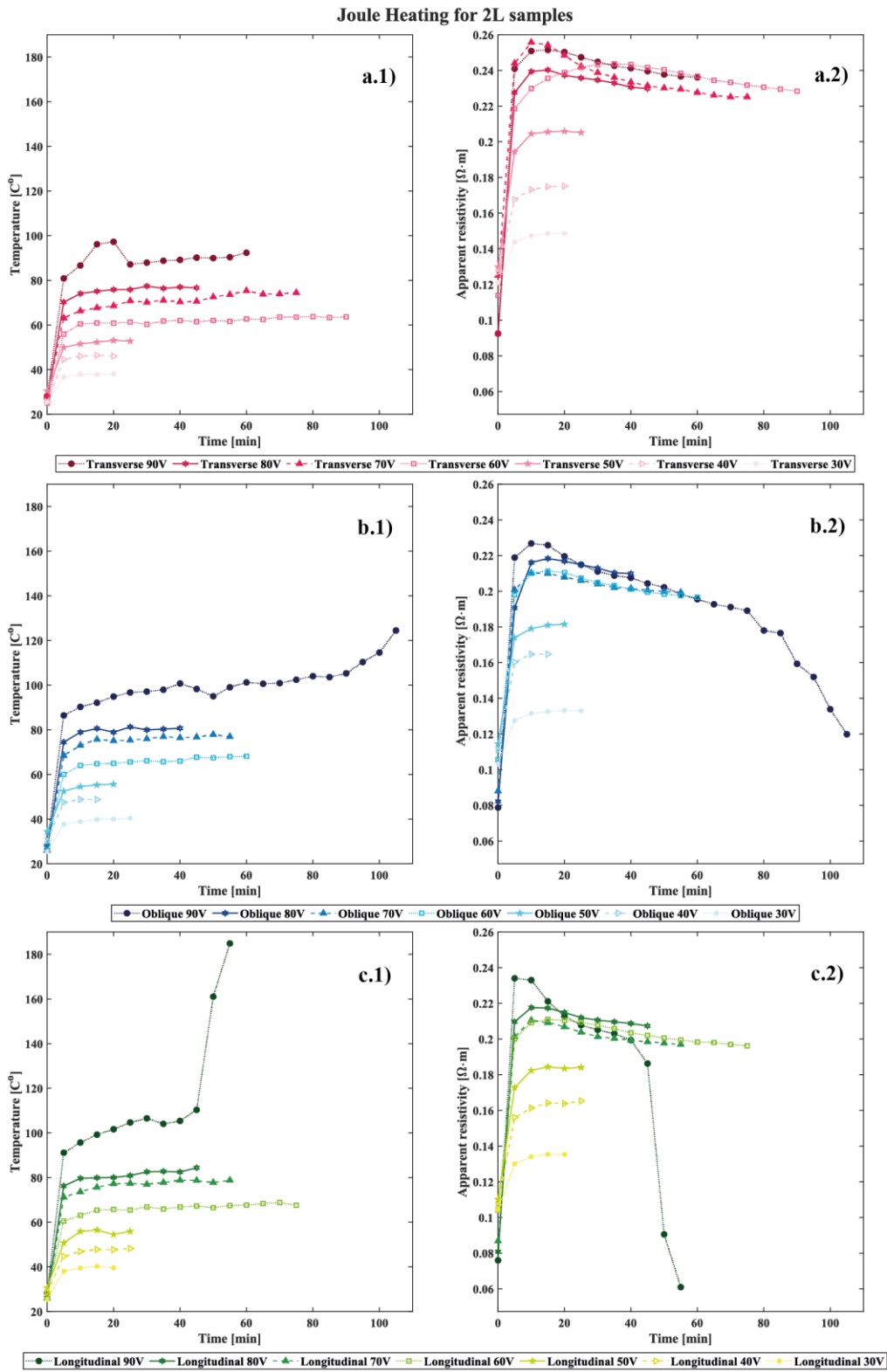
Figure A4: Experimental temperature and resistance results for 2L samples heated by Joule effect imposing seven DC voltages from 30V to 90V a) Transverse samples, b) oblique samples and c) longitudinal samples
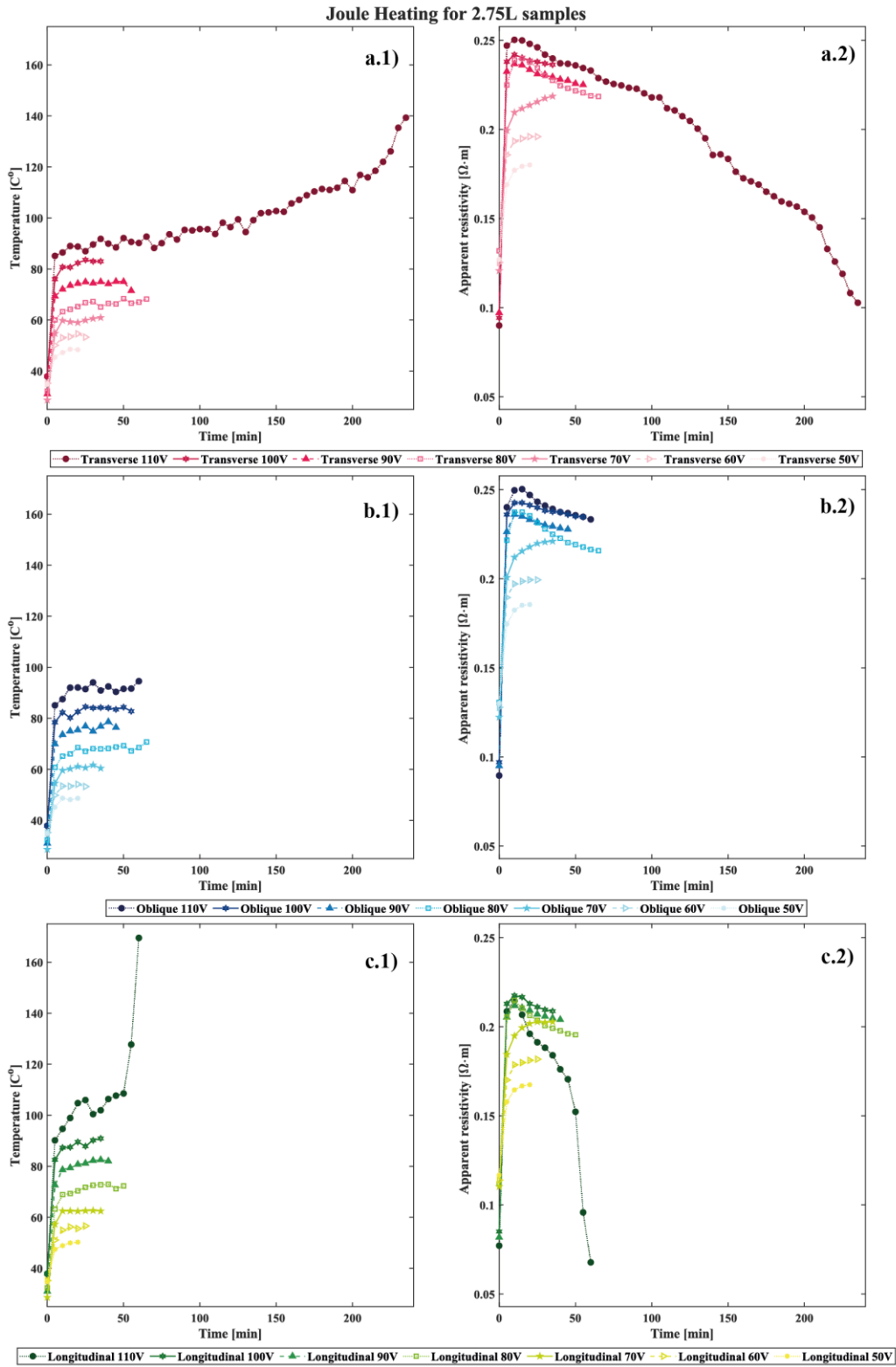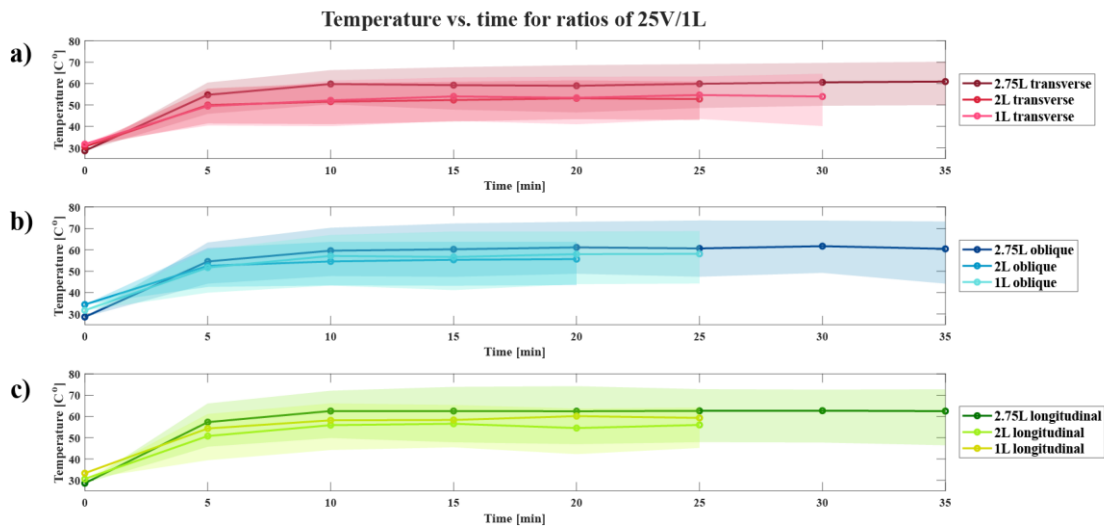
Figure A5: Experimental temperature and resistance results for 1L samples heated by Joule effect imposing seven DC voltages from 50V to 110V. a) Transverse samples, b) oblique samples and c) longitudinal samples

Figure A6: Experimental temperature results for simples with constant ratio of 25V/1L. a) Transverse samples, b) oblique samples, c) longitudinal samples. Solid line represents the average temperature of each sample through time, while shaded area represents maximum and minimum temperature.
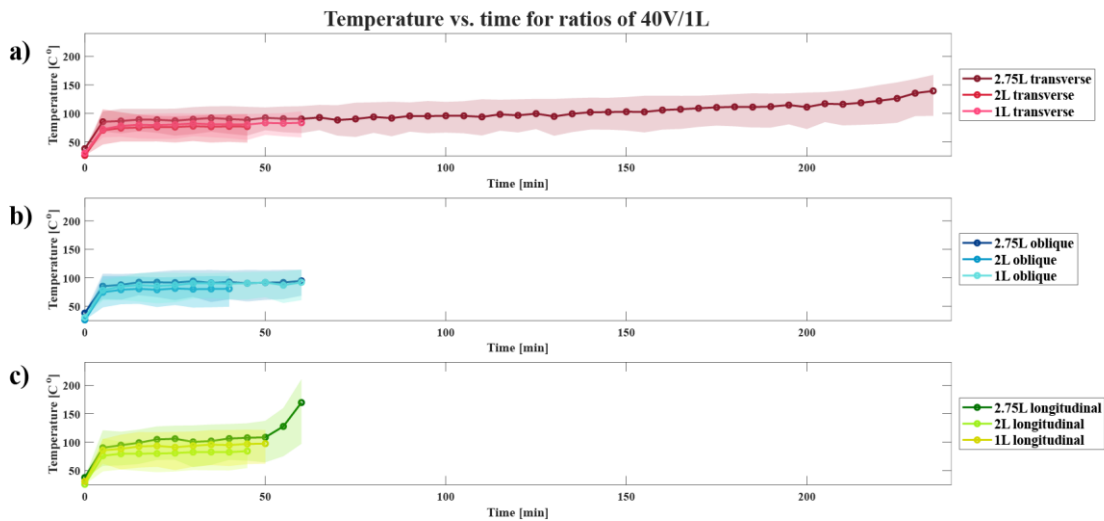

Figure A7: Experimental temperature results for simples with constant ratio of 40V/1L. a) Transverse samples, b) oblique samples, c) longitudinal samples. Solid line represents the average temperature of each sample through time, while shaded area represents maximum and minimum temperature.
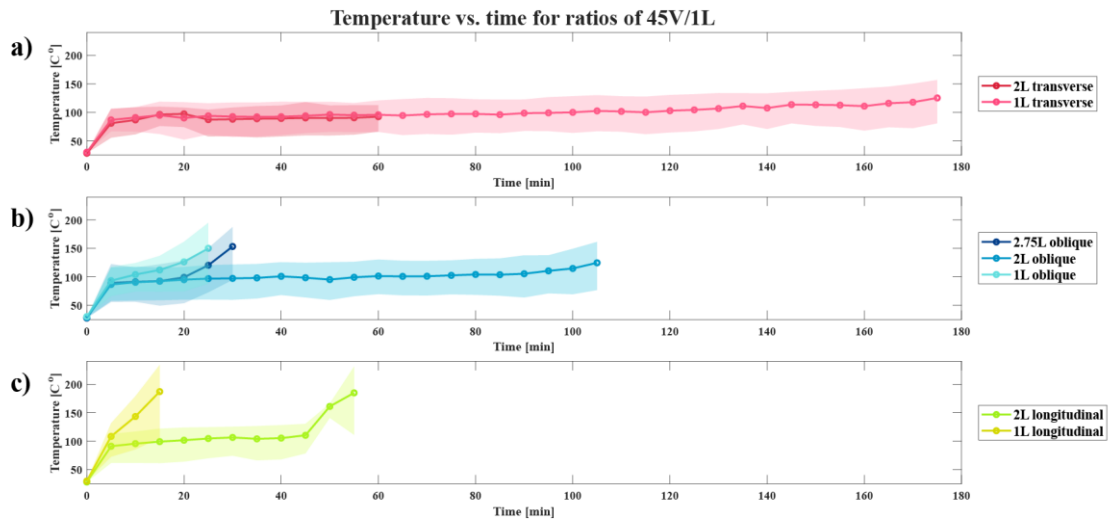
Figure A8: Experimental temperature results for simples with constant ratio of 45V/1L. a) Transverse samples, b) oblique samples, c) longitudinal samples. Solid line represents the average temperature of each sample through time, while shaded area represents maximum and minimum temperature.